

## Silver Nanocubes as Electrochemical Labels for Bioassays

Yi Peng, Charlie Rabin, Charuksha T. Walgama, Nicole E. Pollok, Leilani Smith, Ian Richards, and Richard M. Crooks\*

Cite This: *ACS Sens.* 2021, 6, 1111–1119

Read Online

ACCESS |



Metrics &amp; More



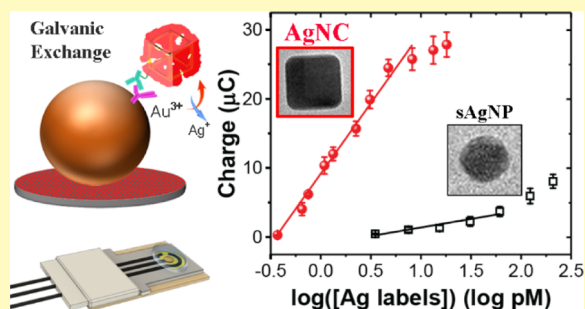
Article Recommendations



Supporting Information

**ABSTRACT:** Here, we report on the use of  $40 \pm 4$  nm silver nanocubes (AgNCs) as electrochemical labels in bioassays. The model metalloimmunoassay combines galvanic exchange (GE) and anodic stripping voltammetry (ASV). The results show that a lower limit of detection is achieved by simply changing the shape of the Ag label yielding improved GE with AgNCs when compared to GE with spherical silver nanoparticles (sAgNPs). Specifically, during GE between electrogenerated  $\text{Au}^{3+}$  and the Ag labels, a thin shell of Au forms on the surface of the NP. This shell is more porous when GE proceeds on AgNCs compared to sAgNPs, and therefore, more exchange occurs when using AgNCs. ASV results show that the Ag collection efficiency (AgCE%) is increased by up to  $\sim 57\%$  when using AgNCs. When the electrochemical system is fully optimized, the limit of detection is 0.1 pM AgNCs, which is an order of magnitude lower than that of sAgNP labels.

**KEYWORDS:** silver nanocube, metalloimmunoassay, galvanic exchange, electrochemical label, paper-based sensor



In this study, we demonstrate the use of silver nanocubes (AgNCs) as electrochemically active labels for detecting a model metalloimmunoassay.<sup>1</sup> The detection method itself is based on electrochemically activated galvanic exchange (GE), followed by anodic stripping voltammetry (ASV).<sup>2–5</sup> The most important finding of this study is that the shape of the Ag label is a key factor for determining the limit of detection (LOD) and the dynamic range of the assay. Specifically, AgNCs provide a LOD 10-fold lower than that of spherical Ag nanoparticles (sAgNPs) for identically prepared assays, but the dynamic range for the AgNCs is significantly smaller. A detailed analysis of the underlying reasons for these observations is presented herein.

Electrochemical bioassays for small molecules, proteins, and nucleic acids, especially those for point-of-care applications, are important diagnostic tools due to their fast response, low cost, and simple operation.<sup>6–9</sup> Stable and robust electrochemical labels play a key role in such assays, especially when the analyte itself is not electrochemically active. Early examples of these types of labels include molecules containing a redox center, such as methylene blue, ferrocene, and thionine.<sup>10–15</sup> These molecules are typically covalently bound to selective biomolecules, such as antibodies (Abs) or DNA, which can recognize and capture an analyte of interest. This type of label is typically present in a 1:1 ratio with the analyte, and therefore, there is no inherent amplification built into the label. This can sometimes, but not always,<sup>16–20</sup> limit their practicality for real-world diagnostic devices. Enzymes, such as alkaline phosphatase and horseradish peroxidase, generate redox-active molecules that are also commonly used as labels in bioassays.<sup>21–24</sup> Enzymes reduce LODs because they are able to produce many

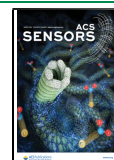
detectable redox molecules per label. However, enzymes can be rather fragile and sensitive to environmental conditions (such as pH and temperature), and the detection time depends on the enzymatic turnover rate which must be tightly controlled.

Inorganic nanomaterials provide an alternative to enzymatic labels. Specifically, electroactive nanomaterials can mimic the amplification function of enzymes while also being more robust and providing faster sample-to-answer times.<sup>25–27</sup> For instance, a seminal article in 2000 reported that spherical Au nanoparticles (sAuNPs) were used as electrochemical labels in a metalloimmunoassay without the incorporation of traditional redox molecules or enzymes.<sup>28</sup> sAuNPs have subsequently been used as electroactive labels in many different types of bioassays.<sup>29–33</sup> More recently, other materials, including sAgNPs<sup>34–38</sup> and quantum dots,<sup>39,40</sup> have also been reported as electrochemical labels for bioassays. Although the approaches cited here overcome the disadvantage of molecular and enzymatic labels, they have their own set of deficiencies. For example, they may require the use of aggressive or hazardous reagents, such as strong acids (e.g.,  $\text{HCl}$ <sup>38</sup> or  $\text{HNO}_3$ )<sup>28,41</sup> or strong oxidizers (e.g.,  $\text{Br}_2$ ,<sup>30</sup>  $\text{KMnO}_4$ ,<sup>1,37</sup> and  $\text{OCI}^-$ )<sup>34</sup> as part of the detection protocol. The steps that require these reagents add

Received: November 13, 2020

Accepted: December 30, 2020

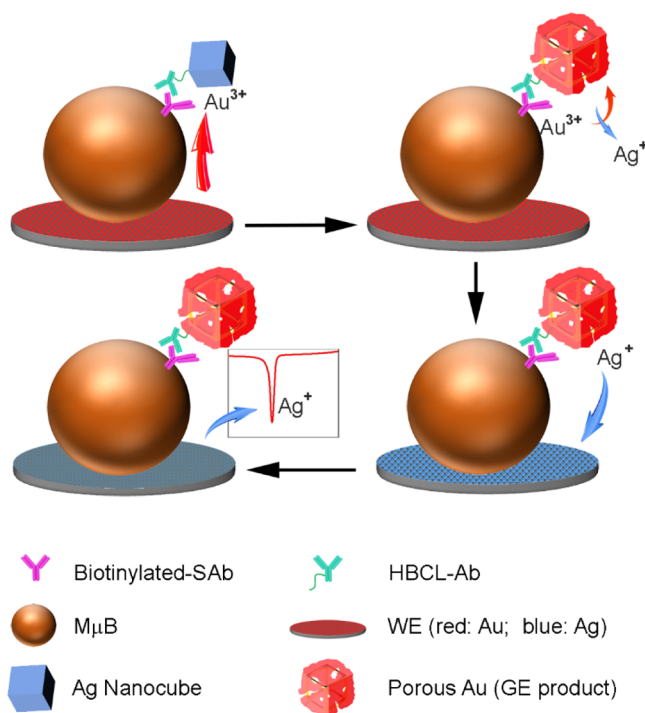
Published: January 13, 2021



complexity and can sometimes damage other components of the detection system.

We recently reported an alternative approach for detecting sAgNP labels that takes advantage of GE and ASV.<sup>2–5</sup> As illustrated in Scheme 1, zero-valent Ag labels are galvanically

**Scheme 1. Schematic Representation of the Electrochemical Detection Process**



exchanged with  $\text{Au}^{3+}$  generated by electro-oxidation of zero-valent Au (previously deposited onto a working electrode, WE). Subsequently,  $\text{Ag}^+$  resulting from GE is electrodeposited onto the WE and then detected by ASV. The efficiency of the GE process is an important parameter, and it is defined as the amount of Ag measured by ASV compared to the total amount of Ag originally present in the labels. We will refer to this parameter as the Ag collection efficiency (AgCE%). The AgCE% is given by eq 1. Here,  $Q$  is the integrated Ag charge in Coulombs recorded during GE,  $F$  is the Faraday constant (96,500 C/mol),  $c$  is the concentration of Ag labels (mol/L),  $N$  is the average number of individual Ag atoms present in a single Ag label, and  $V$  is the volume of the sample.

$$\text{AgCE}\% = \frac{Q}{c \times N \times V \times F} \times 100\% \quad (1)$$

In our previous studies,<sup>3,4</sup> the AgCE% obtained was too low to achieve the necessary LOD for the heart failure bioassay being developed in our lab.<sup>2</sup> Therefore, the objective in this study is to improve the AgCE% and thereby lower the LOD. The guiding hypothesis is that the shape of the Ag labels determines, in part, the AgCE%. Note that in our previous studies<sup>1–5</sup> we used 20 and 110 nm diameter sAgNPs, but we found that simply increasing the particle size did not improve the AgCE%. This was mainly due to the fact that a relatively thick shell of nonporous Au forms around the sAgNP label during GE.<sup>3</sup> This shell prevents complete GE, thereby limiting AgCE%.

The Xia group<sup>42–46</sup> studied the GE of Ag nanocrystals having different morphologies upon the addition of Au salts. A

significant outcome of their work was that the formation of a porous Au shell, which is favorable for maximizing GE, is highly dependent on the morphology of the Ag nanocrystals. Specifically, they found that the GE of AgNCs with  $\text{Au}^{3+}$  leads to the formation of a hollow Au shell that allows the underlying Ag core to be oxidized. This finding inspired us to investigate the performance of AgNCs as electrochemical labels.<sup>3–5</sup> Indeed, we were able to improve our previously optimized AgCE% of 5% (for 110 nm sAgNPs) and 20% (for 20 nm sAgNP) to ~57% by switching to AgNCs.

## EXPERIMENTAL SECTION

**Chemicals.** NaCl, NaOH, HCl,  $\text{KNO}_3$ , sodium citrate, ethylene glycol (EG), Whatman grade 1 chromatography paper (180  $\mu\text{m}$  thick, 20 cm  $\times$  20 cm sheets, linear flow rate of water = 0.43 cm/min), and siliconized low-retention microcentrifuge tubes were purchased from Fisher Scientific (Pittsburgh, PA).  $\text{HAuCl}_4$ , NaSH,  $\text{CF}_3\text{COOAg}$ , phosphate-buffered saline (PBS, pH = 7.4, P3813), bovine serum albumin (BSA), and polyvinylpyrrolidone (PVP, MW ~ 55,000 g/mol) were purchased from Sigma-Aldrich (St Louis, MO). Boric acid was purchased from EM Science (Gibbstown, NJ).

Conductive carbon paste (CI-2042) was purchased from Engineered Conductive Materials (Delaware, OH). Streptavidin-coated, 1.0  $\mu\text{m}$  diameter magnetic beads ( $M\mu\text{Bs}$ , Dynabeads, MyOne Streptavidin T1, 10 mg/mL) were obtained from Invitrogen (Grand Island, NY). Citrate-capped sAgNPs (nominal 20 nm diameter) were purchased from nanoComposix (San Diego, CA). Monoclonal immunoglobulin G anti-NT-proBNP 13G12 (Ab) was obtained from HyTest (Turku, Finland) and biotinylated, polyclonal antimouse immunoglobulin G secondary antibody (SAb) was obtained from Abcam (Cambridge, UK). All solutions were made using deionized (DI) water (>18.0  $\text{M}\Omega\text{-cm}$ , Milli-Q Gradient System, Millipore, Burlington, MA). The buffer was 1 $\times$  PBS.

**Instrumentation.** All electrochemical measurements were carried out using a CHI 760B electrochemical workstation (Austin, TX). The UV–vis spectroscopic measurements were performed using a Hewlett-Packard HP8453 spectrometer with a micro quartz cuvette (50  $\mu\text{L}$ , Hellma, Müllheim, Germany). Inductively coupled plasma mass spectrometry (ICP–MS, 7500ce, Agilent) was used to measure the concentration of the AgNCs.

Transmission electron microscopy (TEM) images were obtained with a JEOL 2010F transmission electron microscope using a voltage of 200 kV. The samples were drop-cast onto Cu grids coated with a carbon film (400 mesh, Electron Microscopy Science) for analysis. A tube revolver (cat. no. 88881001, Thermo Scientific) and a BioShake iQ from Quantifoil Instruments GmbH (Jena, Germany) were used for incubation steps during bioconjugation. Neodymium magnets were purchased from K&J Magnetics (Pipersville, PA) and were used for washing and separating steps involving magnetic microbeads ( $M\mu\text{Bs}$ ).

**Synthesis of AgNCs.** The AgNCs were synthesized using a previously reported method.<sup>47</sup> Briefly, 5.0 mL of 100% EG in a 50 mL round-bottom flask was heated to 150  $^\circ\text{C}$  using an oil bath, and then 60.0  $\mu\text{L}$  of NaSH (3.0 mM in EG) was added. After 2 min, 0.50 mL of HCl (3.0 mM in EG) and 1.25 mL of PVP (20.0 mg/mL in EG) were added. After another 2 min, 0.40 mL of  $\text{CF}_3\text{COOAg}$  (282 mM in EG) was added. The reaction was stopped after 30 min by cooling the flask in an ice bath. The products were washed with acetone and DI water using centrifugation at 12,000g, dispersed in water, and finally stored at 4  $^\circ\text{C}$ . The as-prepared AgNCs were stable for at least 10 weeks with no detectable degradation (as measured by UV–vis spectroscopy, Figure S1a). The atomic Ag concentration was measured by ICP–MS. Various dilutions were prepared based on the ICP–MS results and the corresponding UV–vis spectra were collected, and a corresponding absorbance–concentration calibration plot was prepared, as shown in Figure S2.

**Preparation of Assay Components.** Unless stated otherwise, all reactions were performed at room temperature (RT, 22  $\pm$  3  $^\circ\text{C}$ ). Prior to the conjugation reaction, the AgNCs were washed with a Tween-20

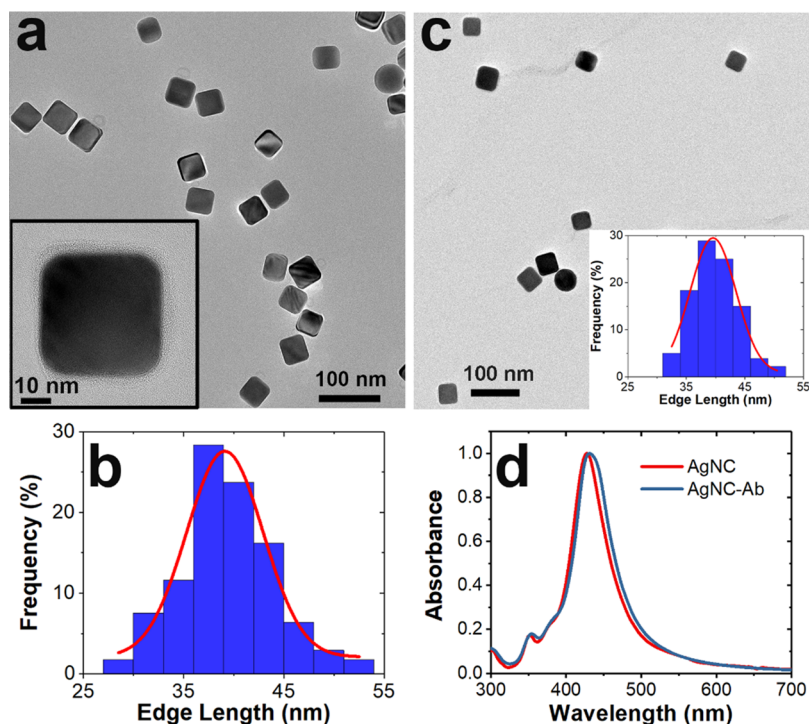


**Figure 1.** Characterization of the AgNC and AgNC-Ab labels. (a) Representative TEM image showing the cubic structure of the AgNCs. The inset is an expanded view of a single AgNC. (b) Histogram of the AgNC edge length obtained by measuring 150 randomly selected AgNC particles. (c) Representative TEM image showing the AgNCs after modification with Abs (AgNC-Abs). The inset is a histogram of AgNC edge length obtained by measuring 100 randomly selected AgNC-Ab particles. (d) UV-vis spectra of solutions of the as-prepared AgNC and AgNC-Ab. All spectra were obtained in aqueous solution using a 50.0  $\mu\text{L}$  cuvette having a 1.00 cm pathlength.

solution (0.01% w/v in water) by centrifugation at 12,000g and then dispersed in a Tween-20 solution. Abs were conjugated to the AgNCs using a previously published protocol with slight modifications.<sup>1</sup> Briefly, the Abs were functionalized with a heterobifunctional cross-linker (HBCL, the detailed procedure can be found in the [Supporting Information](#)). To 500  $\mu\text{L}$  of a AgNC solution ( $6.02 \times 10^{10}$  particles/mL), 25  $\mu\text{L}$  of 1.33  $\mu\text{M}$  Ab-HBCL was added, and the solution was incubated for 1 h in the dark. The excess reagent was then removed by centrifugation for 25 min at 12,000g at 4  $^{\circ}\text{C}$ , and then the conjugates were resuspended in 500  $\mu\text{L}$  of the Tween-20 solution. The resulting product is referred to as AgNC-Ab, and it was stable for at least 21 days without any detectable change as indicated by UV-vis spectroscopy ([Figure S1b](#)). sAgNPs were functionalized with Ab-HBCL using the protocol described in our previous work.<sup>1</sup> These materials are referred to as sAgNP-Ab.

The SAB was conjugated to streptavidin-coated  $M\mu\text{Bs}$  using the protocol provided by the manufacturer.<sup>48</sup> Briefly, 100  $\mu\text{L}$  of  $M\mu\text{Bs}$  ( $\sim 7\text{--}10 \times 10^9$  beads/mL) was washed by magnetic separation three times with PBS. Next, 40.0  $\mu\text{L}$  of 6.67  $\mu\text{M}$  SAB was added and incubated for 30 min in the tube revolver at 30 rpm. Finally, the conjugated  $M\mu\text{Bs}$  were washed by magnetic separation five times with 100  $\mu\text{L}$  of BSA solution (1% w/v in PBS) and resuspended to a final volume of 100  $\mu\text{L}$ . The resulting product is referred to as  $M\mu\text{B-SAB}$ .

The assay components were formed by bioconjugation of  $M\mu\text{B-SAB}$  and AgNC-Ab (or sAgNP-Ab) via the binding between SAB and Ab. Specifically, 16.0  $\mu\text{L}$  of the as-prepared  $M\mu\text{B-SAB}$  was added to 100  $\mu\text{L}$  of AgNC-Ab (or sAgNP-Ab) having the desired concentration and incubated for 1 h in the tube revolver at 30 rpm. The components were washed with PBS five times using magnetic separation, and then they were resuspended in 16.0  $\mu\text{L}$  of PBS. The resulting conjugates are referred to as  $M\mu\text{B-AgNC}$  or  $M\mu\text{B-sAgNP}$ . The final AgNC (or sAgNP) concentration bound to the  $M\mu\text{Bs}$  ( $c_f$ ) can be calculated by eq 2, where  $V_{\text{AgNC}}$  and  $V_{M\mu\text{B}}$  are the volumes of the AgNCs (100  $\mu\text{L}$ ) and the  $M\mu\text{Bs}$  (16  $\mu\text{L}$ ),  $c_i$  is the initial AgNC concentration, and  $c_s$  is the residual AgNC concentration in the supernatant after conjugation. The

values of  $c_i$  and  $c_s$  can be obtained from the absorbance-concentration calibration plot introduced earlier ([Figure S2](#)).

$$c_f = \frac{c_i \times V_{\text{AgNC}} - c_s \times (V_{\text{AgNC}} + V_{M\mu\text{B}})}{V_{M\mu\text{B}}} \quad (2)$$

**Electrode Fabrication.** Electrodes were fabricated using a previously published screen printing method with minor modifications ([Scheme S1](#)).<sup>3</sup> Two different approaches were used to deposit Au onto the WE. The first of these approaches involved the direct drop-cast of 10.0  $\mu\text{L}$  of an optimal concentration of sAuNPs ( $11 \pm 2$  nm diameter, [Figure S3](#))<sup>49</sup> onto the WE and then drying on the benchtop at RT. Hereafter, we refer to this procedure as the “sAuNP drop-cast method”.

The second approach consisted of electrodepositing Au onto the WE using a procedure we have described previously.<sup>2</sup> Specifically, a 50.0  $\mu\text{L}$  droplet of 6.0 mM HAuCl<sub>4</sub> solution (in 0.10 M KNO<sub>3</sub>) was placed on the electrode, and the potential of the WE was stepped from 0 to  $-0.60$  V versus a carbon quasi-reference electrode (CQRE) for 2.0 s. Finally, the electrode was rinsed twice with DI water and dried with a Kimwipe. We refer to this means of depositing Au as the “Au electrodeposition method”.

**Electrochemical Detection.** A NoFlow paper electrochemical device, shown in [Scheme S1](#),<sup>3</sup> was used to analyze the conjugate ( $M\mu\text{B-AgNC}$  or  $M\mu\text{B-sAgNP}$ ) concentrations. This was done according to the following procedure. First, the conjugate was suspended in 2.0  $\mu\text{L}$  of  $M\mu\text{B-AgNC}$  with 48.0  $\mu\text{L}$  of a solution containing 0.10 M borate and 0.10 M NaCl (hereafter, this is referred to as the “BCl solution”). The conjugates were pre-concentrated on the surface of the WE by a magnet positioned under the WE. In this configuration, the WE, the CQRE, and the counter electrode (CE) were all completely covered by the 50  $\mu\text{L}$  droplet of the solution.

The electrochemical protocol used to determine the charge resulting from the process is illustrated in [Scheme 1](#). Specifically, GE was initiated by stepping the potential of the WE from 0 to 0.80 V for 12.0 s to electro-oxidize the zero-valent Au. Next, the WE potential was stepped from 0 to  $-0.70$  V for 75 s (unless specified otherwise) to electrodeposit

the resulting  $\text{Ag}^+$  onto the WE as zero-valent Ag. These steps were carried out twice, and then ASV was used to oxidize Ag, present on the WE, by sweeping the WE potential twice from  $-0.70$  to  $0.20$  V at  $50.0$  mV/s. The area under the second ASV peak was integrated, and the resulting charge correlated to the concentration of the conjugate. Note that all potentials are reported versus the potential of the CQRE unless otherwise indicated.

## RESULTS AND DISCUSSION

**AgNC Characterization.** As discussed in the [Experimental Section](#), the AgNCs used in this study were synthesized using a method reported by Xia and coworkers.<sup>47</sup> Prior to conjugating HBCL-Abs to the AgNCs, the AgNCs were characterized by TEM. Representative TEM images ([Figure 1a](#)) reveal a high yield of AgNCs. An image of a single AgNC is shown in the inset: note the truncated corners. A histogram of the AgNC size ([Figure 1b](#)) was obtained by measuring the edge length of 150 randomly selected AgNCs, and this resulted in a value of  $39 \pm 4$  nm. Using the face-centered-cubic (fcc) Ag lattice constant of  $0.4085$  nm<sup>50</sup> and the average edge length, the number of Ag atoms in an individual AgNC particle is estimated to be  $3.5 \times 10^6$ .

High-resolution TEM (HRTEM) was performed on a selected area on the AgNC surface to clearly show the well-defined Ag lattice fringes ([Figure S4a](#)). The result shows the average lattice spacing of  $0.20$  nm, which is assigned to the (200) facet of fcc Ag (PDF card #4-783). The selected-area electron diffraction pattern ([Figure S4b](#)), obtained by transforming the area in [Figure S4a](#), revealed diffraction spots typical of fcc Ag for the [001] projection. These microscopy results provide a basic understanding of the AgNC structure.

**Conjugation of Abs to AgNCs.** After the AgNCs were fully characterized, they were functionalized with Abs as discussed in the [Experimental Section](#). The conjugation of Abs to the surface of the AgNCs was achieved using the same HBCL linker we have used previously to link Abs to sAgNPs.<sup>1,51</sup> The product of the bioconjugation reaction, AgNC-Ab, was characterized by TEM ([Figure 1c](#)). The histogram in the inset of the figure reveals an average edge length of  $40 \pm 4$  nm, which is not statistically different from the AgNC size obtained prior to functionalization ( $39 \pm 4$  nm). UV-vis spectra of the AgNCs before and after Ab immobilization are shown in [Figure 1d](#). Before functionalization, the peak arising from the localized surface plasmon resonance<sup>52,53</sup> is present at  $428$  nm. After functionalization, this peak experiences a red shift of  $2$ – $5$  nm (depending on the particular synthesis). This small shift results from the change in the refractive index caused by the presence of the Abs.<sup>1,54</sup>

Taken together, the microscopic and spectroscopic results confirm that bioconjugation of Abs to the AgNC surface does not significantly affect the fundamental material properties of the AgNCs.

**Formation of  $M\mu\text{B}$ -AgNC Conjugates.** The  $M\mu\text{B}$ -AgNC conjugate was formed via specific interactions between the Abs on the AgNCs and the SAbS attached to the  $M\mu\text{Bs}$  ([Scheme S2](#)). To confirm the formation of the conjugate, UV-vis spectroscopic measurements were carried out. The black trace in [Figure 2a](#) was obtained from the AgNC-Ab solution, and it reveals a maximum absorption peak at  $\lambda_{\text{max}} = 431$  nm and a concentration of  $12.4$  pM AgNC-Ab. After conjugation and magnetic separation of the  $M\mu\text{B}$ -AgNC conjugates (red trace), the intensity of the peak at  $431$  nm decreased by  $\sim 82\%$ . This indicates that the concentration of unbound AgNC-Ab is  $2.3$  pM. Furthermore, by using [eq 2](#), we find that  $60.8$  pM of the

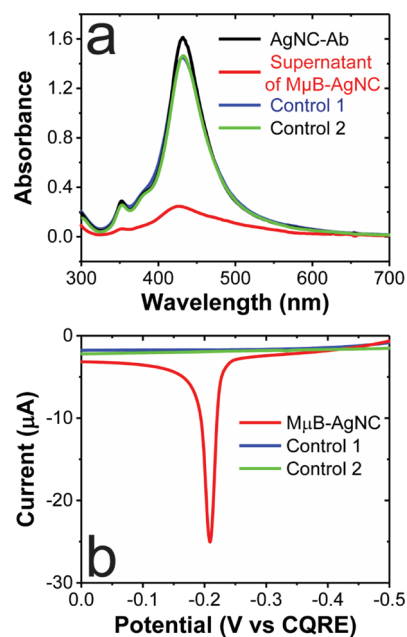


**Figure 2.** Confirmation of formation of the  $M\mu\text{B}$ -AgNC conjugate. (a) UV-vis spectra of the AgNC-Ab conjugate, the supernatant obtained after incubation of AgNC-Ab with  $M\mu\text{B}$ -SAb and magnetic separation, and two control experiments. Control 1 was carried out by incubating unmodified AgNCs (no Abs) with  $M\mu\text{B}$ -SAb, and control 2 was carried out by incubating streptavidin-coated  $M\mu\text{B}$  (no SAbS) with AgNC-Ab, followed, in both cases, by magnetic separation of the  $M\mu\text{Bs}$ . All spectra were obtained in aqueous solution using a  $50.0$   $\mu\text{L}$  cuvette having a  $1.00$  cm pathlength. (b) Electrochemical ASV results for AgNC-Ab conjugates and the same two control experiments in (a). In all cases, the *NoFlow* paper electrochemical cell was used, the electrolyte was  $0.10$  M BCl, and the scan rate was  $50$  mV/s. The spectroscopic and electrochemical measurements were performed in triplicate, and all trials were in accord with those shown in the figure.

AgNC-Ab was bound to the  $M\mu\text{B}$ -SAb. This corresponds to an atomic concentration of Ag of  $212$   $\mu\text{M}$ .

Two control experiments were carried out to check for nonspecific adsorption of AgNCs. Both controls followed the procedure outlined in the previous paragraph but with the following exceptions. For control 1, unmodified AgNCs (no Abs) were used with  $M\mu\text{B}$ -SAb, and in control 2, streptavidin-coated  $M\mu\text{Bs}$  (no SAbS) were used with AgNC-Ab. The absorbances of the supernatants at  $\lambda_{\text{max}}$  (blue and green traces in [Figure 2a](#)) decreased by only  $\sim 11\%$  in both cases. This decrease is due to dilution, however, and therefore, we conclude that there is no detectable nonspecific binding between  $M\mu\text{B}$ -SAb and the unmodified AgNCs or between the streptavidin-modified  $M\mu\text{Bs}$  (no SAbS) and AgNC-Ab.

**Electrochemical Analysis of the  $M\mu\text{B}$ -AgNC Conjugates.** Electrochemical detection of the  $M\mu\text{B}$ -AgNC conjugates was carried out using *NoFlow* paper devices having drop-cast sAuNPs present on the WE. Briefly,  $2.0$   $\mu\text{L}$  of a  $35.6$  pM  $M\mu\text{B}$ -AgNC conjugate solution was diluted with  $48.0$   $\mu\text{L}$  of BCl solution. The concentration of AgNCs in this  $50.0$   $\mu\text{L}$  volume was  $1.4$  pM. This droplet was placed onto the electrode assembly of the *NoFlow* device, which caused the  $M\mu\text{B}$ -AgNC conjugates to concentrate on the WE surface due to the presence of the magnet. After this step was completed, the drop-cast sAuNPs were oxidized for  $12.0$  s, thereby initiating the GE process illustrated in [Scheme 1](#). Next, the resulting  $\text{Ag}^+$  was reduced onto the WE surface for the optimized period of  $75.0$  s ([Figure S5](#)).

Finally, the electrodeposited Ag was electrochemically oxidized by ASV. A representative ASV voltammogram is shown in the red trace in Figure 2b. The average charge collected is  $12.1 \pm 0.8 \mu\text{C}$ . This value can be compared to our previous findings using sAgNPs. In that case, using a similar concentration of 20 nm sAgNP labels,<sup>4</sup> no current was detected. This demonstrates the superiority of AgNCs compared to sAgNPs as electrochemical labels.

We also carried out electrochemical versions of the same two control experiments described in the previous section. In both cases, the same protocol used for the full assay was used for the controls with the exceptions noted earlier. Specifically, control 1 (blue trace in Figure 2b) involved incubation of  $M\mu\text{B}$ -SAb with unmodified AgNCs (no Abs). In this case, no Ag ASV peak was detected. Similarly, for control 2, which involved incubation of streptavidin-coated  $M\mu\text{B}$ s (no SAb) with AgNC-Ab, no ASV peak was detected (green trace in Figure 2b). This confirms the absence of nonspecific adsorption of AgNC onto the  $M\mu\text{B}$ -SAb or AgNC-Ab onto  $M\mu\text{B}$ s (no Abs). These results are fully consistent with the UV-vis data discussed earlier. Accordingly, we conclude that the GE/ASV method is a zero-background measurement.

Additional experiments were performed to assess the stability of the reagent components ( $M\mu\text{B}$ -SAb and AgNC-Ab) and the electrochemical stability of the  $M\mu\text{B}$ -AgNC conjugates. The results, which are provided in Figures S6,S7, indicate that the reagent components and  $M\mu\text{B}$ -AgNC conjugates are stable for at least 21 days.

**Detection of Different  $M\mu\text{B}$ -AgNC Conjugate Concentrations.** Up to this point, experiments were carried out using a single concentration of AgNCs. In real bioassays, however, the number of Ag labels would vary depending upon the concentration of the target analyte. Accordingly, we investigated the relationship between the concentration of AgNCs in  $M\mu\text{B}$ -AgNC conjugates and the resulting electrochemical signal and then compared these results to those obtained using sAgNP labels.

Representative ASV curves for the detection of  $M\mu\text{B}$ -AgNC conjugates incorporating several concentrations of AgNCs are shown in Figure 3a. These results were obtained using drop-cast sAuNPs on the WE surface. Ag charges for many different AgNC concentrations, extracted from data similar to that shown in Figure 3a, are plotted in Figure 3b. These results show that the Ag charge increases with increasing concentration of AgNCs over the range  $\sim 0.4$ – $4.7 \text{ pM}$ . The shape of this curve is characteristic of a Langmuir binding isotherm in that it is linear at low concentrations and then plateaus. A regression analysis of the linear part of the curve indicates a LOD of  $0.1 \text{ pM}$  and a slope of  $7.9 \mu\text{C}/\text{pM}$  at the 95% confidence level.

The same experiment was carried out using electrodeposited Au, rather than drop-cast sAuNPs, as the source of Au for the GE. The ASVs and charge-versus-AgNC concentration data for this experiment are provided in Figure S8. In this case, a similar trend is observed, but the magnitude of the charge for a given AgNC concentration is only about half that is obtained using sAuNPs as the Au source. Accordingly, the LOD and slope in this case are  $0.2 \text{ pM}$  and  $3.2 \mu\text{C}/\text{pM}$ , respectively. These results indicate that the simpler drop-casting method for introducing Au onto the WE surface is slightly more effective than electrodeposition.

When the assay is carried out using sAgNP labels, rather than AgNCs (Figures S9,S10), the LODs are  $1.9$  and  $1.6 \text{ pM}$  when the Au sources for GE are electrodeposited Au and drop-cast

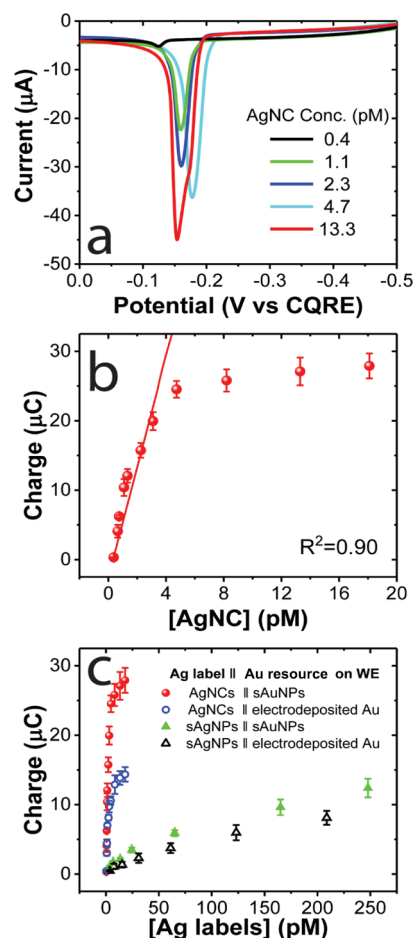


**Figure 3.** Detection of different concentrations of  $M\mu\text{B}$ -AgNC and  $M\mu\text{B}$ -sAgNP conjugates as a function of the Au source. (a) Electrochemical ASV results for  $M\mu\text{B}$ -AgNC conjugates. GE was carried out using drop-cast sAuNPs. (b) Plot of Ag charge, obtained by integrating the area under ASVs like those shown in (a), vs the AgNC concentration. (c) Comparison of the Ag charge collected as a function of the type of Ag label used (AgNCs and sAgNPs), the concentration of the label, and the source of Au used for GE (electrodeposited Au and drop-cast sAuNPs). In (b,c), the error bars represent the standard deviation from the mean for three independent measurements. In all cases, electrochemistry was carried out using the NoFlow paper platform, the electrolyte was  $0.10 \text{ M BCl}$ , and the scan rate was  $50.0 \text{ mV/s}$ .

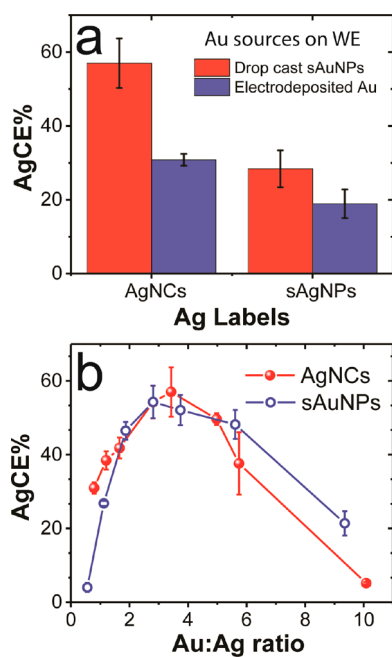
sAuNPs, respectively. These LODs are about an order of magnitude higher than the corresponding values for AgNC labels. The slopes of the plots in Figures S9 and S10 are  $0.07$  and  $0.06$  for electrodeposited Au and drop-cast sAuNPs, respectively. These values are 1 to 2 orders of magnitude smaller than the corresponding plots for the AgNC labels, indicating the improved sensitivity of the analysis when carried out using AgNC labels compared to the sAgNPs.

Figure 3c summarizes the charges recovered for different concentrations of  $M\mu\text{B}$ -AgNCs and  $M\mu\text{B}$ -sAgNPs as a function of the Au source. The results show that, regardless of the Au source, the LODs obtained using the AgNC labels are  $\sim 10$ -fold lower than that of the sAgNPs. Likewise, the detection sensitivity for the AgNC labels is more than a magnitude higher than that for the sAgNPs. Importantly, however, the dynamic range for the sAgNPs is significantly wider regardless of the Au source used for GE. In other words, the AgNC labels lead to a

lower LOD and higher sensitivity than the sAgNPs but at the cost of a restricted dynamic range.

**Insights Regarding the GE Mechanism.** The factors contributing to the differences in the LOD, sensitivity, and dynamic range presented in the previous section are discussed next.

Figure 4a is a histogram comparing the maximum AgCE% for the AgNC and sAgNP labels using either drop-cast sAuNPs or



**Figure 4.** (a) Histograms comparing AgCE% for  $M\mu$ B-AgNCs and  $M\mu$ B-sAgNPs using either drop-cast sAuNPs or electrodeposited Au for GE. (b) Plots of AgCE% vs the Au/Ag ratio. The red plot corresponds to different AgNC concentrations and a constant amount of sAuNP ( $7.5 \times 10^9$  sAuNPs). The blue plot shows how AgCE% changes for different sAuNP concentrations and a constant amount of AgNCs ( $3.91 \times 10^7$  AgNCs or 1.3 pM).

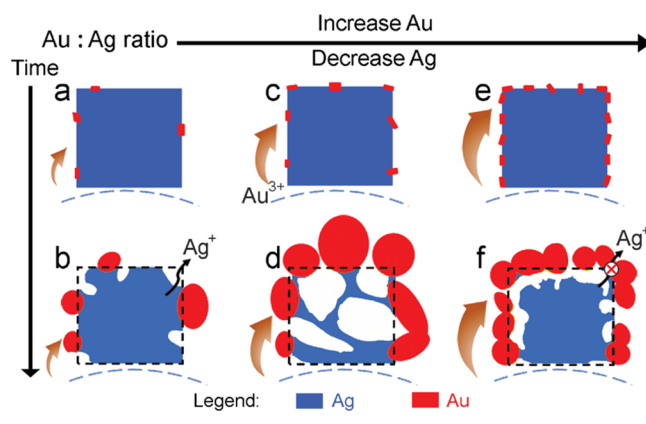
electrodeposited Au as the source of  $Au^{3+}$  for GE. There are two important results. First, the data indicate that regardless of the Ag nanocrystal morphology, the drop-cast sAuNPs lead to a superior GE and hence higher AgCE%. Second, regardless of the type of Au used for GE, the AgNCs provide a higher AgCE% compared to the sAgNP labels.

As shown in Scheme 1, a key step in the detection method is the GE between the Ag labels and  $Au^{3+}$  formed by electro-oxidation of zero-valent Au on the WE. Therefore, the local concentration of  $Au^{3+}$  for each AgNC, in other words the Au/Ag ratio, is an important factor governing the sensitivity of the detection process. This point is underscored by the plots of AgCE% versus the Au/Ag ratio shown in Figure 4b. The red plot is derived from Figure 3b, and it shows how the AgCE% changes as a function of the Au/Ag ratio while keeping the sAuNP concentration constant and varying the concentration of AgNC. The blue plot is the opposite: here, the AgNC concentration is kept constant, while the concentration of the sAuNPs drop-cast onto the WE is varied (these data are derived from Figure S11). The key point is that these two plots have the same general shape and exhibit a similar maximum. This suggests that the Au/Ag ratio, rather than either the concentration of the AgNCs or the sAuNPs alone, controls the AgCE%. A trend similar to that

shown in Figure 4b is observed when electrodeposited Au, rather than drop-cast sAuNPs, is used for GE (Figure S12).

On the basis of previous studies<sup>42–46</sup> and the results shown in Figure 4b, we propose the following mechanism to account for the relationship between AgCE% and the Au/Ag ratio. As shown in the top row of Scheme 2, Ag present on the surface of the

**Scheme 2. Schematic Representation of the GE Detection Process as a Function of Time and the Au:Ag Ratio; (a,b) the AgCE% Is Limited by Insufficient  $Au^{3+}$  per AgNC; This Situation Corresponds to the Left Side of the Plots in Figure 4b; (e,f) a High Au:Ag Ratio (Right Side of the Plots in Figure 4b) Leads to Excess Deposition of Au on the AgNC Surface; the Resulting Au Shell Prevents Full Exchange with Ag in the AgNC Core and Hence a Lower AgCE%; (c,d) an Optimal Au:Ag Ratio Results in the Maximum AgCE%**



AgNCs is oxidized by electrogenerated  $Au^{3+}$ , which itself is reduced to Au on the AgNC surface. The initially deposited Au serves as nucleation sites for subsequent reduction of additional Au.<sup>44,46</sup> Continuation of this process results in a Au shell that partially covers the Ag surface (bottom row of Scheme 2). This inert shell slows the access of  $Au^{3+}$  to the underlying Ag and hence slows the rate of GE. Therefore, when the Au/Ag ratio is low, due to either limited availability of  $Au^{3+}$  or a high concentration of Ag labels, the AgCE% is limited by insufficient  $Au^{3+}$  per AgNC (e.g., Scheme 2a,b). This situation corresponds to the left side of the plots in Figure 4b. In contrast, a high Au/Ag ratio (right side of the plots in Figure 4b) leads to more deposition of Au on the AgNC surface. The resulting Au shell prevents full exchange with Ag in the AgNC core and hence a lower AgCE% (e.g., Scheme 2e,f). Accordingly, there should be an optimal Au/Ag ratio (Scheme 2c,d) that results in a maximum AgCE%. This overall trend is consistent with that shown in Figure 4b.

We now turn our attention to the finding that AgNC labels lead to a higher AgCE% compared to sAgNP labels. We attribute this difference primarily to the nanocube shape, which has previously been shown to form a porous Au shell during the GE process.<sup>42,44</sup> This in turn slows the formation of the Au shell and hence increases the AgCE%. To confirm this hypothesis, STEM images and elemental maps (Figure 5) of the AgNC@Au products were collected after GE. The dark-field STEM image shown in Figure 5a reveals that a shell of Au (bright area) forms around the cubic Ag core (darker region). The bright-field STEM image shown in Figure 5b reveals the porosity (indicated by blue arrows) of the Au shell and the presence of small deposits of Au (red arrows).

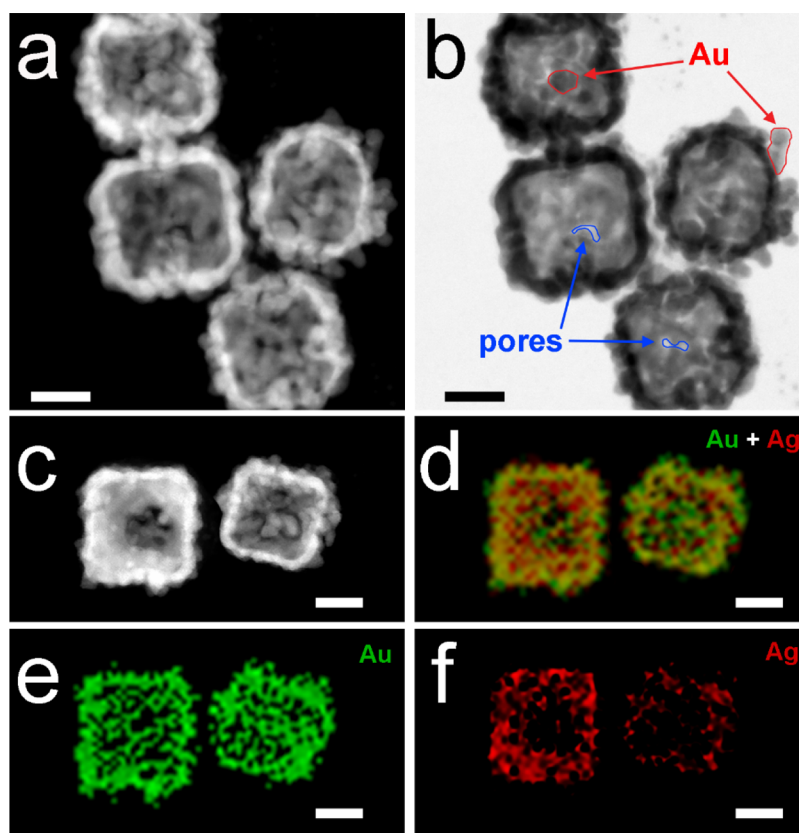


**Figure 5.** STEM and EDS characterization of the AgNCs following GE using sAuNPs as the Au source. The  $M\mu$ Bs were removed from the AgNCs by boiling the sample. The Au/Ag ratio used for GE was 3.4, which corresponds to the maximum AgCE% as shown in Figure 4b. The scale bars are all 25.0 nm. (a) Representative dark-field (DF) and (b) bright-field (BF) STEM images of the AgNCs following GE. (c) DF-STEM image of two randomly selected AgNCs following GE and the corresponding EDS elemental maps of (d) overlay of Au + Ag, (e) Au, and (f) Ag.

EDS elemental maps of AgNCs following GE are shown in Figure 5c–f. These maps clearly show the porosity of the Au shell (Figure 5e) and the low density of Ag in the core (Figure 5f). Moreover, the results in Figure 5 are fully consistent with the structure represented in Scheme 2d, which shows that GE occurs throughout the particle. When the Au/Ag ratio is decreased (left side of the plots shown in Figure 4b), STEM images (Figure S13) are consistent with the structure shown in Scheme 2b. We conclude that the microscopy data confirm the essential features of Scheme 2.

## SUMMARY AND CONCLUSIONS

In summary, we compared the LOD, sensitivity, and dynamic range for an electrochemical immunoassay for two types of labels. The results indicate that  $\sim 40$  nm AgNCs exhibit a 10-fold lower LOD (0.1 pM) compared to  $\sim 20$  nm sAgNP labels (1.9 pM). The main reason for the improvement relates to the higher AgCE% for the AgNCs compared to that for the sAgNPs ( $\sim 57.0\%$  vs 28.4% and 30.8% vs 18.9%, respectively, for drop-cast sAuNPs and electrodeposited Au used for GE). Taken together, these results can be attributed to differences in the GE process for the two different structures. Specifically, the more porous Au shell that forms on the AgNCs results in more exchange of the Ag core.

We are optimistic that these AgCE% improvements will translate well to the ongoing development of a heart failure biosensor being developed in our lab. Specifically, the current performance of this device indicates an LOD that is 5-fold higher than the desirable risk stratification threshold required for

effective clinical applications.<sup>2,55–58</sup> We believe that simply changing the structure of the Ag labels will make it possible to achieve the necessary LOD for real-world applications.

## ASSOCIATED CONTENT

### Supporting Information

The Supporting Information is available free of charge at <https://pubs.acs.org/doi/10.1021/acssensors.0c02377>.

Fabrication of the electrode assembly; schematic illustration of the *NoFlow* paper electrochemical device; synthesis of the heterobifunctional cross-linker (HBCL), synthesis of Ab-HBCL, and schematic illustration showing the synthesis of the  $M\mu$ B-AgNC conjugate; determination of the stability of AgNCs; calibration plot for determining the concentration of Ag; characterization of sAuNPs; microscopic characterization of AgNCs; optimization of the Ag electrodeposition time; stability of the  $M\mu$ B-AgNC conjugates; stability of AgNC-Ab and  $M\mu$ B-SAB; detection of different  $M\mu$ B-AgNC conjugate concentrations using the *NoFlow* paper device and electrodeposited Au for GE; detection of different  $M\mu$ B-sAgNP conjugate concentrations using the *NoFlow* paper device and electrodeposited Au for GE; detection of different  $M\mu$ B-sAgNP conjugate concentrations using the *NoFlow* paper device and drop-cast sAuNPs for GE; optimization of the number of sAuNPs used for GE; plot of AgCE% versus log of the AgNC concentration using the *NoFlow* paper device and electrodeposited Au for GE;

and characterization of the AgNCs following GE and removal of the M $\mu$ Bs (PDF)

## AUTHOR INFORMATION

### Corresponding Author

Richard M. Crooks – Department of Chemistry, The University of Texas at Austin, Austin, Texas 78712-1224, United States; [orcid.org/0000-0001-5186-4878](https://orcid.org/0000-0001-5186-4878); Email: [crooks@cm.utexas.edu](mailto:crooks@cm.utexas.edu)

### Authors

Yi Peng – Department of Chemistry, The University of Texas at Austin, Austin, Texas 78712-1224, United States;

[orcid.org/0000-0002-5319-1336](https://orcid.org/0000-0002-5319-1336)

Charlie Rabin – Department of Chemistry, The University of Texas at Austin, Austin, Texas 78712-1224, United States

Charuksha T. Walgama – Department of Chemistry, The University of Texas at Austin, Austin, Texas 78712-1224, United States; [orcid.org/0000-0002-5549-0436](https://orcid.org/0000-0002-5549-0436)

Nicole E. Pollok – Department of Chemistry, The University of Texas at Austin, Austin, Texas 78712-1224, United States

Leilani Smith – Department of Chemistry, The University of Texas at Austin, Austin, Texas 78712-1224, United States

Ian Richards – Interactives Executive Excellence LLC, Austin, Texas 78733, United States

Complete contact information is available at:

<https://pubs.acs.org/10.1021/acssensors.0c02377>

### Notes

The authors declare the following competing financial interest(s): Richard Crooks and Ian Richards are associated with Galvanix, LLC, and the research reported herein could be useful to this entity in the future.

## ACKNOWLEDGMENTS

The research reported in this publication was supported by the National Heart, Lung, and Blood Institute of the National Institutes of Health under Award R01HL137601. The content is solely the responsibility of the authors and does not necessarily represent the official views of the National Institutes of Health. We also thank the Robert A. Welch Foundation (grant F-0032) for the sustained support of our research. We thank Dr. Karalee Jarvis (UT-Austin) for obtaining the electron microscopy data shown in Figure 5.

## REFERENCES

- (1) Pollok, N. E.; Rabin, C.; Smith, L.; Crooks, R. M. Orientation-Controlled Bioconjugation of Antibodies to Silver Nanoparticles. *Bioconjugate Chem.* **2019**, *30*, 3078–3086.
- (2) Pollok, N. E.; Rabin, C.; Walgama, C. T.; Smith, L.; Richards, I.; Crooks, R. M. Electrochemical Detection of NT-proBNP Using a Metalloimmunoassay on a Paper Electrode Platform. *ACS Sens.* **2020**, *5*, 853–860.
- (3) Kogan, M. R.; Pollok, N. E.; Crooks, R. M. Detection of Silver Nanoparticles by Electrochemically Activated Galvanic Exchange. *Langmuir* **2018**, *34*, 15719–15726.
- (4) Cunningham, J. C.; Kogan, M. R.; Tsai, Y.-J.; Luo, L.; Richards, I.; Crooks, R. M. Paper-Based Sensor for Electrochemical Detection of Silver Nanoparticle Labels by Galvanic Exchange. *ACS Sens.* **2016**, *1*, 40–47.
- (5) Walgama, C.; Nguyen, M. P.; Boatner, L. M.; Richards, I.; Crooks, R. M. Hybrid Paper and 3D-Printed Microfluidic Device for Electrochemical Detection of Ag Nanoparticle Labels. *Lab Chip* **2020**, *20*, 1648–1657.

(6) Labib, M.; Sargent, E. H.; Kelley, S. O. Electrochemical Methods for the Analysis of Clinically Relevant Biomolecules. *Chem. Rev.* **2016**, *116*, 9001–9090.

(7) DeGregory, P. R.; Tapia, J.; Wong, T.; Villa, J.; Richards, I.; Crooks, R. M. Managing Heart Failure at Home With Point-of-Care Diagnostics. *IEEE J. Transl. Eng. Health Med.* **2017**, *5*, 1–6.

(8) Cunningham, J. C.; DeGregory, P. R.; Crooks, R. M. New Functionalities for Paper-Based Sensors Lead to Simplified User Operation, Lower Limits of Detection, and New Applications. *Annu. Rev. Anal. Chem.* **2016**, *9*, 183–202.

(9) Chikkaveeraiah, B. V.; Bhirde, A. A.; Morgan, N. Y.; Eden, H. S.; Chen, X. Electrochemical Immunosensors for Detection of Cancer Protein Biomarkers. *ACS Nano* **2012**, *6*, 6546–6561.

(10) Xiao, Y.; Lubin, A. A.; Baker, B. R.; Plaxco, K. W.; Heeger, A. J. Single-step electronic detection of femtomolar DNA by target-induced strand displacement in an electrode-bound duplex. *Proc. Natl. Acad. Sci. U.S.A.* **2006**, *103*, 16677–16680.

(11) Li, J.; Sun, M.; Wei, X.; Zhang, L.; Zhang, Y. An electrochemical aptamer biosensor based on “gate-controlled” effect using  $\beta$ -cyclodextrin for ultra-sensitive detection of trace mercury. *Biosens. Bioelectron.* **2015**, *74*, 423–426.

(12) Martić, S.; Labib, M.; Shipman, P. O.; Kraatz, H.-B. Ferrocene-peptide conjugates: from synthesis to sensory applications. *Dalton Trans.* **2011**, *40*, 7264–7290.

(13) Hu, J.; Wang, T.; Kim, J.; Shannon, C.; Easley, C. J. Quantitation of Femtomolar Protein Levels via Direct Readout with the Electrochemical Proximity Assay. *J. Am. Chem. Soc.* **2012**, *134*, 7066–7072.

(14) Vallée-Bélisle, A.; Ricci, F.; Uzawa, T.; Xia, F.; Plaxco, K. W. Bioelectrochemical Switches for the Quantitative Detection of Antibodies Directly in Whole Blood. *J. Am. Chem. Soc.* **2012**, *134*, 15197–15200.

(15) Mars, A.; Ben jaafar, S.; Gaied, A. B. A.-E.; Raouafi, N. Electrochemical immunoassay for lactalbumin based on the use of ferrocene-modified gold nanoparticles and lysozyme-modified magnetic beads. *Microchim. Acta* **2018**, *185*, 449.

(16) Li, H.; Somerson, J.; Xia, F.; Plaxco, K. W. Electrochemical DNA-Based Sensors for Molecular Quality Control: Continuous, Real-Time Melamine Detection in Flowing Whole Milk. *Anal. Chem.* **2018**, *90*, 10641–10645.

(17) Ogden, N. E.; Kurnik, M.; Parolo, C.; Plaxco, K. W. An electrochemical scaffold sensor for rapid syphilis diagnosis. *Analyst* **2019**, *144*, 5277–5283.

(18) Idili, A.; Parolo, C.; Ortega, G.; Plaxco, K. W. Calibration-Free Measurement of Phenylalanine Levels in the Blood Using an Electrochemical Aptamer-Based Sensor Suitable for Point-of-Care Applications. *ACS Sens.* **2019**, *4*, 3227–3233.

(19) Ricci, F.; Vallée-Bélisle, A.; Simon, A. J.; Porchetta, A.; Plaxco, K. W. Using Nature’s “Tricks” To Rationally Tune the Binding Properties of Biomolecular Receptors. *Acc. Chem. Res.* **2016**, *49*, 1884–1892.

(20) Hsieh, K.; Ferguson, B. S.; Eisenstein, M.; Plaxco, K. W.; Soh, H. T. Integrated Electrochemical Microsystems for Genetic Detection of Pathogens at the Point of Care. *Acc. Chem. Res.* **2015**, *48*, 911–920.

(21) Das, J.; Jo, K.; Lee, J. W.; Yang, H. Electrochemical Immunosensor Using p-Aminophenol Redox Cycling by Hydrazine Combined with a Low Background Current. *Anal. Chem.* **2007**, *79*, 2790–2796.

(22) Tang, J.; Tang, D.; Niessner, R.; Chen, G.; Knopp, D. Magneto-Controlled Graphene Immunosensing Platform for Simultaneous Multiplexed Electrochemical Immunoassay Using Distinguishable Signal Tags. *Anal. Chem.* **2011**, *83*, 5407–5414.

(23) Sarkar, P.; Ghosh, D.; Bhattacharyay, D.; Setford, S. J.; Turner, A. P. F. Electrochemical Immunoassay for Free Prostate Specific Antigen (f-PSA) Using Magnetic Beads. *Electroanalysis* **2008**, *20*, 1414–1420.

(24) Fu, Y.; Wang, N.; Yang, A.; Law, H. K.-w.; Li, L.; Yan, F. Highly Sensitive Detection of Protein Biomarkers with Organic Electrochemical Transistors. *Adv. Mater.* **2017**, *29*, 1703787.

(25) Lei, J.; Ju, H. Signal amplification using functional nanomaterials for biosensing. *Chem. Soc. Rev.* **2012**, *41*, 2122–2134.

- (26) Wongkaew, N.; Simsek, M.; Griesche, C.; Baumner, A. J. Functional Nanomaterials and Nanostructures Enhancing Electrochemical Biosensors and Lab-on-a-Chip Performances: Recent Progress, Applications, and Future Perspective. *Chem. Rev.* **2019**, *119*, 120–194.
- (27) Liu, G.; Lin, Y. Nanomaterial labels in electrochemical immunosensors and immunoassays. *Talanta* **2007**, *74*, 308–317.
- (28) Dequaire, M.; Degrand, C.; Limoges, B. An electrochemical metalloimmunoassay based on a colloidal gold label. *Anal. Chem.* **2000**, *72*, 5521–5528.
- (29) Kawde, A.-N.; Wang, J. Amplified Electrical Transduction of DNA Hybridization Based on Polymeric Beads Loaded with Multiple Gold Nanoparticle Tags. *Electroanalysis* **2004**, *16*, 101–107.
- (30) Wang, J.; Xu, D.; Kawde, A.-N.; Polsky, R. Metal Nanoparticle-Based Electrochemical Stripping Potentiometric Detection of DNA Hybridization. *Anal. Chem.* **2001**, *73*, 5576–5581.
- (31) López-Marzo, A. M.; Hoyos-de-la-Torre, R.; Baldrich, E. NaNO<sub>3</sub>/NaCl Oxidant and Polyethylene Glycol (PEG) Capped Gold Nanoparticles (AuNPs) as a Novel Green Route for AuNPs Detection in Electrochemical Biosensors. *Anal. Chem.* **2018**, *90*, 4010–4018.
- (32) Zhou, W.; Gao, X.; Liu, D.; Chen, X. Gold Nanoparticles for In Vitro Diagnostics. *Chem. Rev.* **2015**, *115*, 10575–10636.
- (33) Fan, A.; Lau, C.; Lu, J. Magnetic Bead-Based Chemiluminescent Metal Immunoassay with a Colloidal Gold Label. *Anal. Chem.* **2005**, *77*, 3238–3242.
- (34) Cunningham, J. C.; Scida, K.; Kogan, M. R.; Wang, B.; Ellington, A. D.; Crooks, R. M. Paper diagnostic device for quantitative electrochemical detection of ricin at picomolar levels. *Lab Chip* **2015**, *15*, 3707–3715.
- (35) Li, X.; Scida, K.; Crooks, R. M. Detection of Hepatitis B Virus DNA with a Paper Electrochemical Sensor. *Anal. Chem.* **2015**, *87*, 9009–9015.
- (36) Liu, G.; Wang, J.; Kim, J.; Jan, M. R.; Collins, G. E. Electrochemical Coding for Multiplexed Immunoassays of Proteins. *Anal. Chem.* **2004**, *76*, 7126–7130.
- (37) Scida, K.; Cunningham, J. C.; Renault, C.; Richards, I.; Crooks, R. M. Simple, Sensitive, and Quantitative Electrochemical Detection Method for Paper Analytical Devices. *Anal. Chem.* **2014**, *86*, 6501–6507.
- (38) Wang, J.; Liu, G.; Wu, H.; Lin, Y. Quantum-Dot-Based Electrochemical Immunoassay for High-Throughput Screening of the Prostate-Specific Antigen. *Small* **2008**, *4*, 82–86.
- (39) Boriachek, K.; Islam, M. N.; Gopalan, V.; Lam, A. K.; Nguyen, N.-T.; Shiddiky, M. J. A. Quantum dot-based sensitive detection of disease specific exosome in serum. *Analyst* **2017**, *142*, 2211–2219.
- (40) Shiddiky, M. J. A.; Rauf, S.; Kithva, P. H.; Trau, M. Graphene/quantum dot bionanoconjugates as signal amplifiers in stripping voltammetric detection of EpCAM biomarkers. *Biosens. Bioelectron.* **2012**, *35*, 251–257.
- (41) Cai, H.; Xu, Y.; Zhu, N.; He, P.; Fang, Y. An electrochemical DNA hybridization detection assay based on a silver nanoparticle label. *Analyst* **2002**, *127*, 803–808.
- (42) Chen, J.; McLellan, J. M.; Siekkinen, A.; Xiong, Y.; Li, Z.-Y.; Xia, Y. Facile Synthesis of Gold–Silver Nanocages with Controllable Pores on the Surface. *J. Am. Chem. Soc.* **2006**, *128*, 14776–14777.
- (43) Skrabalak, S. E.; Au, L.; Li, X.; Xia, Y. Facile synthesis of Ag nanocubes and Au nanocages. *Nat. Protoc.* **2007**, *2*, 2182–2190.
- (44) Au, L.; Lu, X.; Xia, Y. A comparative study of galvanic replacement reactions involving Ag nanocubes and AuCl<sub>2</sub><sup>-</sup> or AuCl<sub>4</sub><sup>-</sup>. *Adv. Mater.* **2008**, *20*, 2517–2522.
- (45) Lu, X.; Au, L.; McLellan, J.; Li, Z.-Y.; Marquez, M.; Xia, Y. Fabrication of Cubic Nanocages and Nanoframes by Dealloying Au/Ag Alloy Nanoboxes with an Aqueous Etchant Based on Fe(NO<sub>3</sub>)<sub>3</sub> or NH<sub>4</sub>OH. *Nano Lett.* **2007**, *7*, 1764–1769.
- (46) Sun, Y.; Mayers, B. T.; Xia, Y. Template-Engaged Replacement Reaction: A One-Step Approach to the Large-Scale Synthesis of Metal Nanostructures with Hollow Interiors. *Nano Lett.* **2002**, *2*, 481–485.
- (47) Zhang, Q.; Li, W.; Wen, L.-P.; Chen, J.; Xia, Y. Facile Synthesis of Ag Nanocubes of 30 to 70 nm in Edge Length with CF<sub>3</sub>COOAg as a Precursor. *Chem.—Eur. J.* **2010**, *16*, 10234–10239.
- (48) Thermo Fisher *Dynabeads MyOne Streptavidin T1 Protocol*, 2016.
- (49) Peng, Y.; Li, L.; Mu, X.; Guo, L. Aptamer-gold nanoparticle-based colorimetric assay for the sensitive detection of thrombin. *Sens. Actuators, B* **2013**, *177*, 818–825.
- (50) Davey, W. P. Precision Measurements of the Lattice Constants of Twelve Common Metals. *Phys. Rev.* **1925**, *25*, 753–761.
- (51) Kumar, S.; Aaron, J.; Sokolov, K. Directional conjugation of antibodies to nanoparticles for synthesis of multiplexed optical contrast agents with both delivery and targeting moieties. *Nat. Protoc.* **2008**, *3*, 314–320.
- (52) Krenn, J. R. Nanoparticle waveguides - Watching energy transfer. *Nat. Mater.* **2003**, *2*, 210–211.
- (53) Mock, J. J.; Smith, D. R.; Schultz, S. Local refractive index dependence of plasmon resonance spectra from individual nanoparticles. *Nano Lett.* **2003**, *3*, 485–491.
- (54) Khlebtsov, N. G. Determination of size and concentration of gold nanoparticles from extinction spectra. *Anal. Chem.* **2008**, *80*, 6620–6625.
- (55) Januzzi, J. L.; Troughton, R. Are Serial BNP Measurements Useful in Heart Failure Management? *Circulation* **2013**, *127*, 500–508.
- (56) Masson, S.; Latini, R.; Anand, I. S.; Vago, T.; Angelici, L.; Barlera, S.; Missov, E. D.; Clerico, A.; Tognoni, G.; Cohn, J. N. Direct comparison of B-type natriuretic peptide (BNP) and amino-terminal proBNP in a large population of patients with chronic and symptomatic heart failure: the Valsartan Heart Failure (Val-HeFT) data. *Clin. Chem.* **2006**, *52*, 1528–1538.
- (57) Felker, G. M.; Ahmad, T.; Anstrom, K. J.; Adams, K. F.; Cooper, L. S.; Ezekowitz, J. A.; Fiuzat, M.; Houston-Miller, N.; Januzzi, J. L.; Leifer, E. S.; Mark, D. B.; Desvigne-Nickens, P.; Paynter, G.; Piña, I. L.; Whellan, D. J.; O'Connor, C. M. Rationale and design of the GUIDE-IT study: guiding evidence based therapy using biomarker intensified treatment in heart failure. *JACC Heart Fail.* **2014**, *2*, 457–465.
- (58) Zile, M. R.; Claggett, B. L.; Prescott, M. F.; McMurray, J. J. V.; Packer, M.; Rouleau, J. L.; Swedberg, K.; Desai, A. S.; Gong, J.; Shi, V. C.; Solomon, S. D. Prognostic Implications of Changes in N-Terminal Pro-B-Type Natriuretic Peptide in Patients With Heart Failure. *J. Am. Coll. Cardiol.* **2016**, *68*, 2425–2436.